

A spectral-element discontinuous Galerkin lattice Boltzmann method for nearly incompressible flows

Misun Min^a, Taehun Lee^{b,*}

^a Mathematics and Computer Science Division, Argonne National Laboratory, Argonne, IL 60439, USA

^b Department of Mechanical Engineering, City College of City University of New York, New York, NY 10031, USA

ARTICLE INFO

Article history:

Received 24 October 2009

Received in revised form 20 September 2010

Accepted 20 September 2010

Available online 29 September 2010

Keywords:

Lattice Boltzmann method

Spectral element method

Discontinuous Galerkin method

ABSTRACT

We present a spectral-element discontinuous Galerkin lattice Boltzmann method for solving nearly incompressible flows. Decoupling the collision step from the streaming step offers numerical stability at high Reynolds numbers. In the streaming step, we employ high-order spectral-element discontinuous Galerkin discretizations using a tensor product basis of one-dimensional Lagrange interpolation polynomials based on Gauss–Lobatto–Legendre grids. Our scheme is cost-effective with a fully diagonal mass matrix, advancing time integration with the fourth-order Runge–Kutta method. We present a consistent treatment for imposing boundary conditions with a numerical flux in the discontinuous Galerkin approach. We show convergence studies for Couette flows and demonstrate two benchmark cases with lid-driven cavity flows for $Re = 400$ – 5000 and flows around an impulsively started cylinder for $Re = 550$ – 9500 . Computational results are compared with those of other theoretical and computational work that used a multigrid method, a vortex method, and a spectral element model.

© 2010 Elsevier Inc. All rights reserved.

1. Introduction

The lattice Boltzmann method (LBM) has been successfully applied to many computational fluid dynamics problems over the past two decades [1,2]. The lattice Boltzmann equation (LBE) is a special discrete form of the Boltzmann equation from kinetic theory. LBE simulates the weakly compressible Navier–Stokes equations, but the incompressible Navier–Stokes equations can be derived from LBE through the Chapman–Enskog expansion if the Mach number (Ma) and the density fluctuation are on the order of $O(\varepsilon)$ and $O(\varepsilon^2)$, respectively, where ε is the Knudsen number [3]. The use of a small velocity expansion in the derivation of the Navier–Stokes equations from LBE makes LBM valid in the low Ma regime.

In the conventional LBM, the streaming of the particle distribution function is given as the exact solution of linear advection equation so that it offers exact numerical solutions. Severe limitations arise, however, from the use of uniform Cartesian grids and its inherent instability at high Reynolds number (Re). These two aspects are closely related to each other in that LBE is a discretized form of the discrete Boltzmann equation (DBE) along characteristics, and thus the time and space discretizations are strongly coupled. Since He and Luo [4] and Abe [5] demonstrated that the discretization of physical space does not necessarily need to couple with the discretization of momentum space, several efforts have been made to address the treatment of curved or irregular boundaries and the control of mesh resolution at desirable regions, and significant progress has been achieved in recent years to overcome the limitations of LBM. With a rigorous foundation established, various numerical methods have been applied directly to the discrete Boltzmann equation (DBE) using finite difference (FD)

* Corresponding author. Tel.: +1 212 650 6122; fax: +1 212 650 8013.

E-mail addresses: mmin@mcs.anl.gov (M. Min), thlee@ccny.cuny.edu (T. Lee).

[6–13], finite volume (FV) [14–18], finite element (FE) [19–21], and spectral-element discontinuous Galerkin (SEDG) methods [22,23].

FD-LBM is a straightforward generalization of the conventional LBM at non-unit *CFL* (Courant–Friedrich–Lewy) number [24]. The perfect shift in the conventional LBM is a special case of FD-LBM at unit *CFL* number. The simple Cartesian grid structure for FD-LBM offers ease of implementation but complicates accurate treatment of curved boundaries, causing unwanted velocity slip and mass and momentum conservation errors [25,26]. The spatial approximation of FV-LBM uses local approximation in space and imposes no conditions on the grid structure; thus, the approach is suitable for dealing with complex geometries. From the divergence theorem, the flux term of DBE becomes surface integral, requiring local reconstruction of the fluxes at the boundaries. However, when we need to increase the order of accuracy, a high-order reconstruction of the solution values at the interface introduce difficulties with geometric flexibility [27]. On the contrary, FE-LBM allows higher-order approximation simply by adding additional degrees of freedom to the element, while retaining geometric flexibility. In FE-LBM, the solution is continuous on the nodes along the faces of the elements shared by the neighboring elements, which essentially introduces the globally defined basis and test functions. The inversion of global mass matrix can be expensive, however, when a fully explicit time-stepping method is employed.

In this paper, we present SEDG-LBM using quadrilateral elements based on Gauss–Lobatto–Legendre grids for which the two-dimensional mass matrix becomes a complete diagonal matrix whose inversion is trivial. We use an explicit Runge–Kutta method for time-stepping. In [22,23], SEDG-LBMs based on triangular meshes are applied to the complete DBE. In our SEDG-LBM, we split our scheme into collision and streaming step. The SEDG approximation is applied to the streaming step of LBE after the collision step is completed. This enables our approach to avoid the severe time-step restriction caused by small values of the relaxation time and helps us investigate flows at higher Reynolds number.

We examine central and upwind numerical fluxes for the numerical flux in discontinuous Galerkin approach. For the particle distribution function that enters into the computational domain, a boundary condition needs to be provided. We use the bounce-back scheme [28], in which the incoming particle distribution function into the domain takes the value of the outgoing particle distribution function in the opposite direction. In [23], the bounce-back rule was imposed strongly on the incoming particle distribution function after each time-step. In the present work, the bounce-back scheme is implemented in a weak sense through the numerical flux, which is consistent with the overall numerical procedure inside the computational domain.

The paper is organized as follows. In Section 2, we present the LBE for the nearly incompressible flows and the SEDG approximation applied to the LBE. Spatial and temporal discretizations are detailed, and numerical fluxes for wall boundary conditions are discussed. Section 3 is devoted to validation of our SEDG-LBM. The physics of lid-driven cavity flows and impulsively started flows past a circular cylinder are studied. Conclusions are given in Section 4.

2. Formulation

In this section, we derive LBE by discretizing DBE along characteristics, which is solved in two steps: collision and streaming. For the streaming step, we examine a discontinuous Galerkin approach based on spectral element discretization using quadrilateral elements in two dimensions. We construct numerical fluxes and present a consistent treatment for imposing boundary conditions with the central and Lax–Friedrichs fluxes. Spatial and temporal discretizations are discussed in detail.

2.1. Lattice Boltzmann equation

We consider the DBE with the Bhatnagar–Gross–Krook collision operator [29] written as:

$$\frac{\partial f_\alpha}{\partial t} + \mathbf{e}_\alpha \cdot \nabla f_\alpha = -\frac{f_\alpha - f_\alpha^{eq}}{\lambda} \quad \text{on } \Omega \quad \text{for } \alpha = 0, 1, \dots, N_\alpha, \quad (1)$$

where f_α is the particle distribution function defined in the direction of the microscopic velocity \mathbf{e}_α , λ is the relaxation time, and N_α is the number of microscopic velocities. Here we consider a two-dimensional 9-velocity model given as $\mathbf{e}_\alpha = (0, 0)$ for $\alpha = 0$; $\mathbf{e}_\alpha = (\cos \theta_\alpha, \sin \theta_\alpha)$ for $\alpha = 1, 2, 3, 4$ and $\mathbf{e}_\alpha = \sqrt{2}(\cos \theta_\alpha, \sin \theta_\alpha)$ for $\alpha = 5, 6, 7, 8$, where $\theta_\alpha = (\alpha - 1)\pi/4$. The equilibrium distribution function is given by

$$f_\alpha^{eq} = t_\alpha \rho \left[1 + \frac{\mathbf{e}_\alpha \cdot \mathbf{u}}{c_s^2} + \frac{(\mathbf{e}_\alpha \cdot \mathbf{u})^2}{2c_s^4} - \frac{(\mathbf{u} \cdot \mathbf{u})}{2c_s^2} \right], \quad (2)$$

where ρ is the density, \mathbf{u} is the macroscopic velocity, $t_0 = 4/9$, $t_{\alpha=1,4} = 1/9$, and $t_{\alpha=5,8} = 1/36$ are the weights, and $c_s = 1/\sqrt{3}$ is the speed of sound [30].

The LBE is obtained by discretizing Eq. (1) along characteristics over the time-step δt as:

$$f_\alpha(\mathbf{x}, t) - f_\alpha(\mathbf{x} - \mathbf{e}_\alpha \delta t, t - \delta t) = - \int_{t-\delta t}^t \frac{f_\alpha - f_\alpha^{eq}}{\lambda} dt', \quad (3)$$

in which time integration over $[t - \delta t, t]$ is coupled with space integration in $[\mathbf{x} - \mathbf{e}_\alpha \delta t, \mathbf{x}]$. Taking a second-order approximation by the trapezoidal rule for the integration in the right-hand side of Eq. (3), we have

$$f_\alpha(\mathbf{x}, t) - f_\alpha(\mathbf{x} - \mathbf{e}_\alpha \delta t, t - \delta t) = -\frac{f_\alpha - f_\alpha^{eq}}{2\tau} \Big|_{(\mathbf{x} - \mathbf{e}_\alpha \delta t, t - \delta t)} - \frac{f_\alpha - f_\alpha^{eq}}{2\tau} \Big|_{(\mathbf{x}, t)}, \tag{4}$$

where the dimensionless relaxation time is $\tau = \lambda/\delta t$ with a relation to the kinematic viscosity by $\nu = \tau c_s^2 \delta t$.

Here, we introduce a modified particle distribution function \bar{f}_α and its corresponding equilibrium distribution function \bar{f}_α^{eq} in order to facilitate computation by transforming the implicitly coupled LBE into an explicit LBE [31]:

$$\bar{f}_\alpha = f_\alpha + \frac{f_\alpha - f_\alpha^{eq}}{2\tau} \quad \text{and} \quad \bar{f}_\alpha^{eq} = f_\alpha^{eq}. \tag{5}$$

Then Eq. (4) can be recast in a simpler form in terms of the modified particle distribution function:

$$\bar{f}_\alpha(\mathbf{x}, t) - \bar{f}_\alpha(\mathbf{x} - \mathbf{e}_\alpha \delta t, t - \delta t) = -\frac{1}{\tau + 1/2} (\bar{f}_\alpha - \bar{f}_\alpha^{eq}) \Big|_{(\mathbf{x} - \mathbf{e}_\alpha \delta t, t - \delta t)}. \tag{6}$$

While Eq. (6) appears to be explicit in time, it is fully implicit for the collision term.

We solve Eq. (6) in two steps:

- Collision

$$\check{f}_\alpha(\mathbf{x}, t - \delta t) = \bar{f}_\alpha(\mathbf{x}, t - \delta t) - \frac{1}{\tau + 1/2} (\bar{f}_\alpha - \bar{f}_\alpha^{eq}) \Big|_{(\mathbf{x}, t - \delta t)}, \tag{7}$$

which is followed by the substitution $\bar{f}_\alpha(\mathbf{x}, t - \delta t) = \check{f}_\alpha(\mathbf{x}, t - \delta t)$.

- Streaming

$$\bar{f}_\alpha(\mathbf{x}, t) = \bar{f}_\alpha(\mathbf{x} - \mathbf{e}_\alpha \delta t, t - \delta t). \tag{8}$$

The density and momentum can be computed by taking moments as follows:

$$\rho = \sum_{\alpha=0}^{N_\alpha} \bar{f}_\alpha, \quad \text{and} \quad \rho \mathbf{u} = \sum_{\alpha=0}^{N_\alpha} \mathbf{e}_\alpha \bar{f}_\alpha. \tag{9}$$

Eq. (8) is the exact solution of pure advection equation, but it is only neutrally stable and restricted to uniform square mesh at unit CFL number such that both (\mathbf{x}) and $(\mathbf{x} - \mathbf{e}_\alpha \delta t)$ reside on the nodal points of the mesh. Alternatively, the streaming step can be expressed as a solution of the pure advection equation in an Eulerian framework [20], which can be expressed as follows.

- Solution of advection equation

$$\frac{\partial \bar{f}_\alpha}{\partial t} + \mathbf{e}_\alpha \cdot \nabla \bar{f}_\alpha = 0 \tag{10}$$

Note that the factor 1/2 in the collision term of Eq. (7) is due to the implicit treatment. As the Reynolds number increases, the dimensionless relaxation time $\tau = \nu/(c_s^2 \delta t)$ approaches zero, but the collision step remains stable because of the factor 1/2, although oscillatory solution may develop as the amplification factor turns negative [20]. If we solve Eq. (1) without splitting it into two steps and treat the collision term explicitly [22,23], the collision term does not include the factor 1/2 and becomes singular at high Reynolds number, thus severely restricting the maximum allowable time-step size. Second-order extrapolation [9,21] and predictor–corrector methods [19] have been proposed to discretize the nonlinear collision operator to increase the maximum time-step, but they are generally less stable.

2.2. Spectral element discontinuous Galerkin method

We begin this section with a weak formulation of the advection equation, Eq. (10), using a discontinuous Galerkin approach introducing flux vector. Spectral element discretizations, numerical fluxes with boundary condition implementation, and time integration are discussed.

2.2.1. Weak formulation for the discontinuous Galerkin method

A multidomain approach for solving the advection equation is used. We consider a nonoverlapping element Ω^e such that $\Omega = \cup_{e=1}^E \Omega^e$. We introduce a flux vector defined as $\mathbf{F}_\alpha(\bar{f}) = \mathbf{e}_\alpha \bar{f}_\alpha$ for the microscopic velocity vector $\mathbf{e}_\alpha = (e_{\alpha x}, e_{\alpha y})$. Then Eq. (10) defined on Ω can be written as:

$$\frac{\partial \bar{f}_\alpha}{\partial t} + \nabla \cdot \mathbf{F}_\alpha(\bar{f}) = 0. \tag{11}$$

Eq. (11) can be recast in an equivalent variational form as:

$$\left(\frac{\partial \bar{f}_\alpha}{\partial t} + \nabla \cdot \mathbf{F}_\alpha(\bar{f}), \phi \right)_{\Omega^e} = 0, \tag{12}$$

where ϕ is a local test function. Integrating by parts of Eq. (12), we obtain

$$\int_{\Omega^e} \phi \frac{\partial \bar{f}_\alpha}{\partial t} d\Omega - \int_{\Omega^e} \mathbf{F}_\alpha(\bar{f}) \cdot \nabla \phi d\Omega = - \int_{\partial\Omega^e} \phi \mathbf{n} \cdot \mathbf{F}_\alpha(\bar{f}) d\bar{\Omega}, \tag{13}$$

where $\bar{\Omega}$ represents the surface boundary of the element Ω^e (i.e., $\partial\Omega^e$) and $\mathbf{n} = (n_x, n_y)$ is the unit normal vector pointing outward. Here we introduce a numerical flux \mathbf{F}^* , which is a function of the local solution \bar{f} and the neighboring solution \bar{f}^+ at the interfaces between neighboring elements. The numerical flux combines the two solutions that are allowed to be different at the neighboring element interfaces. The analytic flux $\mathbf{F}_\alpha(\bar{f})$ is replaced by the numerical flux $\mathbf{F}_\alpha^*(\bar{f})$:

$$\int_{\Omega^e} \phi \frac{\partial \bar{f}_\alpha}{\partial t} d\Omega - \int_{\Omega^e} \mathbf{F}_\alpha(\bar{f}) \cdot \nabla \phi d\Omega = - \int_{\partial\Omega^e} \phi \mathbf{n} \cdot \mathbf{F}_\alpha^*(\bar{f}) d\bar{\Omega}. \tag{14}$$

Integrating by parts of Eq. (14) again, we obtain the final form of the weak formulation as follows:

$$\left(\frac{\partial \bar{f}_\alpha}{\partial t} + \nabla \cdot \mathbf{F}_\alpha(\bar{f}), \phi \right)_{\Omega^e} = (\mathbf{n} \cdot [\mathbf{F}_\alpha(\bar{f}) - \mathbf{F}_\alpha^*(\bar{f})], \phi)_{\partial\Omega^e}. \tag{15}$$

2.2.2. Numerical fluxes for the discontinuous Galerkin method

We define two different numerical fluxes, namely, central and Lax–Friedrichs fluxes for $\mathbf{F}_\alpha^*(\bar{f}) = \mathbf{F}_\alpha^*(\bar{f}, \bar{f}^+)$.

(i) Central Flux

For the central flux given by

$$\mathbf{F}_\alpha^*(\bar{f}, \bar{f}^+) = \frac{1}{2} [\mathbf{F}_\alpha(\bar{f}) + \mathbf{F}_\alpha(\bar{f}^+)], \tag{16}$$

we have the following form in the integrand of Eq. (15):

$$\mathbf{n} \cdot (\mathbf{F}_\alpha - \mathbf{F}_\alpha^*) = \frac{1}{2} (\mathbf{n} \cdot \mathbf{e}_x) [\bar{f}_\alpha - \bar{f}_\alpha^+] = \frac{1}{2} (n_x e_{xx} + n_y e_{xy}) [\bar{f}_\alpha - \bar{f}_\alpha^+]. \tag{17}$$

At the interfaces, the normal vectors hold $n_x = -n_x^+$ and $n_y = -n_y^+$. However, the components of the velocity vector are always fixed in the neighboring element for each \mathbf{e}_x . Thus Eq. (17) can be separated into two components: one for local component and the other for neighboring component with “+”:

$$\mathbf{n} \cdot (\mathbf{F}_\alpha - \mathbf{F}_\alpha^*) = \frac{1}{2} [(n_x e_{xx} + n_y e_{xy}) \bar{f}_\alpha + (n_x^+ e_{xx} + n_y^+ e_{xy}) \bar{f}_\alpha^+]. \tag{18}$$

(ii) Lax–Friedrichs Flux

For the Lax–Friedrichs flux [27,32,33], we have

$$\mathbf{F}_\alpha^*(\bar{f}, \bar{f}^+) = \frac{1}{2} [\mathbf{F}_\alpha(\bar{f}) + \mathbf{F}_\alpha(\bar{f}^+) + |\Lambda| (\bar{f}_\alpha - \bar{f}_\alpha^+) \mathbf{n}], \tag{19}$$

where $\Lambda = \max(\mathbf{n} \cdot \frac{\partial \mathbf{F}}{\partial \mathbf{f}}) = \mathbf{n} \cdot \mathbf{e}_x$. We have the following form in the integrand of Eq. (15):

$$\mathbf{n} \cdot (\mathbf{F}_\alpha - \mathbf{F}_\alpha^*) = \frac{1}{2} (\mathbf{n} \cdot \mathbf{e}_x - |\mathbf{n} \cdot \mathbf{e}_x|) [\bar{f}_\alpha - \bar{f}_\alpha^+], \tag{20}$$

which can be simplified as:

$$\mathbf{n} \cdot (\mathbf{F}_\alpha - \mathbf{F}_\alpha^*) = \begin{cases} (\mathbf{n} \cdot \mathbf{e}_x) [\bar{f}_\alpha - \bar{f}_\alpha^+] & \text{for } \mathbf{n} \cdot \mathbf{e}_x < 0, \\ 0 & \text{for } \mathbf{n} \cdot \mathbf{e}_x \geq 0. \end{cases} \tag{21}$$

In a similar manner to that in (18), for the case of $\mathbf{n} \cdot \mathbf{e}_x < 0$, we can write

$$\mathbf{n} \cdot (\mathbf{F}_\alpha - \mathbf{F}_\alpha^*) = (n_x e_{xx} + n_y e_{xy}) \bar{f}_\alpha + (n_x^+ e_{xx} + n_y^+ e_{xy}) \bar{f}_\alpha^+. \tag{22}$$

2.2.3. Boundary conditions

Wall boundary conditions are weakly imposed through the numerical fluxes. For outgoing particle distribution functions with $\mathbf{e}_x \cdot \mathbf{n} > 0$, the flux difference is set to be $\bar{f}_\alpha - \bar{f}_\alpha^+ = 0$. For incoming particle distribution functions with $\mathbf{e}_x \cdot \mathbf{n} < 0$, we apply boundary conditions through $\bar{f}_\alpha - \bar{f}_\alpha^+ = \bar{f}_\alpha - \bar{f}_{\alpha'} - 2t_x \rho_0 (\mathbf{e}_x \cdot \mathbf{u}_b) / c_s^2$, where $\bar{f}_{\alpha'}$ is the particle distribution function moving in the opposite direction of \bar{f}_α , \mathbf{u}_b is the macroscopic velocity prescribed at the wall boundary, and ρ_0 is the reference density that is chosen to be unity. The detailed expression for the flux difference in Eqs. (17) and (21) in the two-dimensional 9-velocity model can be written as follows:

$$\begin{aligned}
 \text{if } \mathbf{e}_1 \cdot \mathbf{n} < 0 \quad (\iff \mathbf{e}_3 \cdot \mathbf{n} > 0); \quad & \bar{f}_1 - \bar{f}_1^+ = [\bar{f}_1 - \bar{f}_3] - 2t_1\rho_0(\mathbf{e}_1 \cdot \mathbf{u}_b)/c_s^2, \\
 & \bar{f}_3 - \bar{f}_3^+ = [\bar{f}_3 - \bar{f}_1] = 0, \\
 \text{if } \mathbf{e}_2 \cdot \mathbf{n} < 0 \quad (\iff \mathbf{e}_4 \cdot \mathbf{n} > 0); \quad & \bar{f}_2 - \bar{f}_2^+ = [\bar{f}_2 - \bar{f}_4] - 2t_2\rho_0(\mathbf{e}_2 \cdot \mathbf{u}_b)/c_s^2, \\
 & \bar{f}_4 - \bar{f}_4^+ = [\bar{f}_4 - \bar{f}_2] = 0, \\
 \text{if } \mathbf{e}_3 \cdot \mathbf{n} < 0 \quad (\iff \mathbf{e}_1 \cdot \mathbf{n} > 0); \quad & \bar{f}_3 - \bar{f}_3^+ = [\bar{f}_3 - \bar{f}_1] - 2t_3\rho_0(\mathbf{e}_3 \cdot \mathbf{u}_b)/c_s^2, \\
 & \bar{f}_1 - \bar{f}_1^+ = [\bar{f}_1 - \bar{f}_3] = 0, \\
 \text{if } \mathbf{e}_4 \cdot \mathbf{n} < 0 \quad (\iff \mathbf{e}_2 \cdot \mathbf{n} > 0); \quad & \bar{f}_4 - \bar{f}_4^+ = [\bar{f}_4 - \bar{f}_2] - 2t_4\rho_0(\mathbf{e}_4 \cdot \mathbf{u}_b)/c_s^2, \\
 & \bar{f}_2 - \bar{f}_2^+ = [\bar{f}_2 - \bar{f}_4] = 0, \\
 \text{if } \mathbf{e}_5 \cdot \mathbf{n} < 0 \quad (\iff \mathbf{e}_7 \cdot \mathbf{n} > 0); \quad & \bar{f}_5 - \bar{f}_5^+ = [\bar{f}_5 - \bar{f}_7] - 2t_5\rho_0(\mathbf{e}_5 \cdot \mathbf{u}_b)/c_s^2, \\
 & \bar{f}_7 - \bar{f}_7^+ = [\bar{f}_7 - \bar{f}_5] = 0, \\
 \text{if } \mathbf{e}_6 \cdot \mathbf{n} < 0 \quad (\iff \mathbf{e}_8 \cdot \mathbf{n} > 0); \quad & \bar{f}_6 - \bar{f}_6^+ = [\bar{f}_6 - \bar{f}_8] - 2t_6\rho_0(\mathbf{e}_6 \cdot \mathbf{u}_b)/c_s^2, \\
 & \bar{f}_8 - \bar{f}_8^+ = [\bar{f}_8 - \bar{f}_6] = 0, \\
 \text{if } \mathbf{e}_7 \cdot \mathbf{n} < 0 \quad (\iff \mathbf{e}_5 \cdot \mathbf{n} > 0); \quad & \bar{f}_7 - \bar{f}_7^+ = [\bar{f}_7 - \bar{f}_5] - 2t_7\rho_0(\mathbf{e}_7 \cdot \mathbf{u}_b)/c_s^2, \\
 & \bar{f}_5 - \bar{f}_5^+ = [\bar{f}_5 - \bar{f}_7] = 0, \\
 \text{if } \mathbf{e}_8 \cdot \mathbf{n} < 0 \quad (\iff \mathbf{e}_3 \cdot \mathbf{n} > 0); \quad & \bar{f}_8 - \bar{f}_8^+ = [\bar{f}_8 - \bar{f}_6] - 2t_8\rho_0(\mathbf{e}_8 \cdot \mathbf{u}_b)/c_s^2, \\
 & \bar{f}_6 - \bar{f}_6^+ = [\bar{f}_6 - \bar{f}_8] = 0.
 \end{aligned}$$

2.2.4. Spectral element discretizations

We use a tensor product basis of the one-dimensional Legendre–Lagrange interpolation polynomials given as:

$$l_i(\xi) = N(N + 1)^{-1}(1 - \xi^2)L'_N(\xi)/(\xi - \xi_i)L_N(\xi_i) \quad \text{for } \xi \in [-1, 1], \tag{23}$$

where ξ_i is the Gauss–Lobatto–Legendre (GLL) quadrature nodes. Now we consider our computational domain Ω in two-dimensional space. Each $(x, y) \in \Omega^e$ is mapped on the reference domain, $(\xi, \eta) \in I = [-1, 1]^2$, through a Gordon–Hall mapping [34]. The tensor-product structure of the reference element I allows us to define a two-dimensional basis as $\psi_{ij}(\xi, \eta) = l_i(\xi(x))l_j(\eta(y))$, or simply ψ_{ij} .

We seek a local approximate solution in Ω^e defined by the finite expansion of the tensor product basis $\psi_{ij}(\xi, \eta)$ as:

$$\bar{f}_\alpha^N(x, y, t) = \sum_{ij=0}^N (\bar{F}_\alpha^N)_{ij} \psi_{ij}(\xi, \eta), \tag{24}$$

where $(\bar{F}_\alpha^N)_{ij} = \bar{f}_\alpha^N(x_i, y_j, t)$, that is, the nodal values of the approximate solution \bar{f}_α^N at time t on the tensor product of the one-dimensional GLL quadrature nodes, (ξ_i, η_j) [34,35].

For derivatives, we have

$$\frac{\partial \bar{f}_\alpha^N}{\partial t} = \sum_{ij=0}^N \frac{d(\bar{F}_\alpha^N)_{ij}}{dt} \psi_{ij}(\xi, \eta), \tag{25}$$

$$\frac{\partial \bar{f}_\alpha^N}{\partial x} = \sum_{ij=0}^N (\bar{F}_\alpha^N)_{ij} \frac{\partial \psi_{ij}}{\partial x}(\xi, \eta) = \sum_{ij=0}^N (\bar{F}_\alpha^N)_{ij} \left(\frac{\partial \psi_{ij}}{\partial \xi} \frac{\partial \xi}{\partial x} + \frac{\partial \psi_{ij}}{\partial \eta} \frac{\partial \eta}{\partial x} \right), \tag{26}$$

$$\frac{\partial \bar{f}_\alpha^N}{\partial y} = \sum_{ij=0}^N (\bar{F}_\alpha^N)_{ij} \frac{\partial \psi_{ij}}{\partial y}(\xi, \eta) = \sum_{ij=0}^N (\bar{F}_\alpha^N)_{ij} \left(\frac{\partial \psi_{ij}}{\partial \xi} \frac{\partial \xi}{\partial y} + \frac{\partial \psi_{ij}}{\partial \eta} \frac{\partial \eta}{\partial y} \right), \tag{27}$$

where we can compute the geometric terms pointwise by

$$\frac{\partial \xi}{\partial x} = \frac{1}{J} \frac{\partial y}{\partial \eta}, \quad \frac{\partial \eta}{\partial x} = -\frac{1}{J} \frac{\partial y}{\partial \xi}, \quad \frac{\partial \xi}{\partial y} = -\frac{1}{J} \frac{\partial x}{\partial \eta}, \quad \frac{\partial \eta}{\partial y} = \frac{1}{J} \frac{\partial x}{\partial \xi}, \tag{28}$$

with the Jacobian $J = \left(\frac{\partial x}{\partial \xi} \frac{\partial y}{\partial \eta} - \frac{\partial x}{\partial \eta} \frac{\partial y}{\partial \xi} \right)$ from the following relation:

$$\begin{pmatrix} \frac{\partial \xi}{\partial x} & \frac{\partial \xi}{\partial y} \\ \frac{\partial \eta}{\partial x} & \frac{\partial \eta}{\partial y} \end{pmatrix} \begin{pmatrix} \frac{\partial x}{\partial \xi} & \frac{\partial x}{\partial \eta} \\ \frac{\partial y}{\partial \xi} & \frac{\partial y}{\partial \eta} \end{pmatrix} \equiv \begin{pmatrix} 1 & 0 \\ 0 & 1 \end{pmatrix}. \tag{29}$$

We recall the weak formulation Eq. (15) and substitute Eqs. (24)–(27) into it, with a test function chosen from the tensor product basis, namely, $\phi := \psi_{ij}$. Then we have the following components in the discretized weak form:

$$\frac{d(\bar{f}_\alpha^N)_{ij}}{dt}(\psi_{ij}, \psi_{ij})_{\Omega^e} + e_{\alpha x}(\bar{f}_\alpha^N)_{ij} \left(\frac{\partial \psi_{ij}}{\partial x}, \psi_{ij} \right)_{\Omega^e} + e_{\alpha y}(\bar{f}_\alpha^N)_{ij} \left(\frac{\partial \psi_{ij}}{\partial y}, \psi_{ij} \right)_{\Omega^e} = \left(\mathbf{n} \cdot \left[\mathbf{F}(\bar{f}_\alpha^N)_{ij} - \mathbf{F}^*(\bar{f}_\alpha^N)_{ij} \right], \psi_{ij} \right)_{\partial \Omega^e}. \tag{30}$$

Applying the Gauss quadrature rule to Eq. (30), we obtain the mass and stiffness matrices in two dimensions. For the mass matrix, we have

$$\mathbf{M} = (\psi_{ij}, \psi_{ij})_{\Omega^e} = \sum_{k=0}^N \sum_{m=0}^N J_{km} w_k w_m l_i(\xi_k) l_i(\xi_k) l_j(\eta_m) l_j(\eta_m) = J(\widehat{\mathbf{M}} \otimes \widehat{\mathbf{M}}), \tag{31}$$

where w_k is the quadrature weights, J_{km} is the value at each node in a local element for the Jacobian J , and $\widehat{\mathbf{M}} = [\widehat{M}_{ij}] = \sum_{k=0}^N w_k l_i(\xi_k) l_i(\xi_k)$ is the one-dimensional mass matrix defined on the reference domain $[-1, 1]$. Because of the orthogonal property of the Lagrange interpolation polynomials, the one-dimensional mass matrix is a diagonal matrix, resulting in a complete diagonal matrix also in two dimensions. The gradient matrices are represented in a tensor product form of the one-dimensional differentiation matrix $\widehat{\mathbf{D}} = [\widehat{D}_{ij}] = l_j(\xi_i)$ as:

$$\begin{aligned} \mathbf{D}_x &= \left(\frac{\partial \psi_{ij}}{\partial x}, \psi_{ij} \right) = \sum_{k=0}^N \sum_{m=0}^N G_{km}^{x\zeta} J_{km} w_k w_m l_i(\xi_k) l_i'(\xi_k) l_j(\eta_m) l_j(\eta_m) + \sum_{k=0}^N \sum_{m=0}^N G_{km}^{\eta\zeta} J_{km} w_k w_m l_i(\xi_k) l_i(\xi_k) l_j(\eta_m) l_j'(\eta_m) \\ &= G^{x\zeta} J[\widehat{\mathbf{M}} \otimes \widehat{\mathbf{M}} \widehat{\mathbf{D}}] + G^{\eta\zeta} J[\widehat{\mathbf{M}} \widehat{\mathbf{D}} \otimes \widehat{\mathbf{M}}], \end{aligned} \tag{32}$$

$$\begin{aligned} \mathbf{D}_y &= \left(\frac{\partial \psi_{ij}}{\partial y}, \psi_{ij} \right) = \sum_{k=0}^N \sum_{m=0}^N G_{km}^{y\eta} J_{km} w_k w_m l_i(\xi_k) l_i(\xi_k) l_j(\eta_m) l_j'(\eta_m) + \sum_{k=0}^N \sum_{m=0}^N G_{km}^{\xi\eta} J_{km} w_k w_m l_i(\xi_k) l_i'(\xi_k) l_j(\eta_m) l_j(\eta_m) \\ &= G^{y\eta} J[\widehat{\mathbf{M}} \otimes \widehat{\mathbf{M}} \widehat{\mathbf{D}}] + G^{\xi\eta} J[\widehat{\mathbf{M}} \widehat{\mathbf{D}} \otimes \widehat{\mathbf{M}}], \end{aligned} \tag{33}$$

where $G^{x\zeta} = \text{diag}(G_{km}^{x\zeta})$, $G^{y\eta} = \text{diag}(G_{km}^{y\eta})$, $G^{\eta\zeta} = \text{diag}(G_{km}^{\eta\zeta})$, and $G^{\xi\eta} = \text{diag}(G_{km}^{\xi\eta})$ represent the geometric factors $\frac{\partial \zeta}{\partial x}$, $\frac{\partial \zeta}{\partial y}$, $\frac{\partial \eta}{\partial x}$, and $\frac{\partial \eta}{\partial y}$, respectively, and their values at each node (ξ_k, η_m) .

The surface integration in Eq. (31) is in fact the one-dimensional integration on each face of the local element:

$$\mathbf{R}(\bar{f}_\alpha^N) = \sum_{s=1}^4 \sum_{k=0}^N \mathcal{R}_k^s \left\{ \left(\mathbf{n} \cdot \mathbf{e}_\alpha \right) \left[(\bar{f}_\alpha^N)_{ij} - (\bar{f}_\alpha^N)_{ij}^+ \right] \right\} w_k J_k^s, \tag{34}$$

where $\mathcal{R}_k^s \{ \cdot \}$ extracts the information of $\{ \cdot \}$ at the nodes situated on each face of the local element for the face number s and J_k^s is the surface Jacobian at the nodes on each face. To define the unit normal vector \mathbf{n} corresponding to the face in the reference domain I with respect to ζ and η , i.e., \mathbf{n}_ζ and \mathbf{n}_η , respectively, we consider the infinitesimal displacement (x, y) in the tangential direction along the boundary $\partial \Omega^e$, which can be written as:

$$\epsilon_\zeta = \left(\frac{\partial x}{\partial \zeta}, \frac{\partial y}{\partial \zeta} \right) d\zeta, \quad \text{and} \quad \epsilon_\eta = \left(\frac{\partial x}{\partial \eta}, \frac{\partial y}{\partial \eta} \right) d\eta. \tag{35}$$

From the fact that $\frac{\partial \zeta}{\partial x} \frac{\partial x}{\partial \eta} + \frac{\partial \zeta}{\partial y} \frac{\partial y}{\partial \eta} = \frac{\partial \eta}{\partial x} \frac{\partial x}{\partial \zeta} + \frac{\partial \eta}{\partial y} \frac{\partial y}{\partial \zeta} = 0$ in Eq. (29) and the relation in Eq. (28), we can obtain the normal vectors as:

$$\hat{\mathbf{n}}_\zeta = \left(\frac{\partial \eta}{\partial x}, \frac{\partial \eta}{\partial y} \right) = \frac{1}{J} \left(\frac{\partial y}{\partial \eta}, -\frac{\partial x}{\partial \eta} \right), \quad \hat{\mathbf{n}}_\eta = \left(\frac{\partial x}{\partial \zeta}, \frac{\partial x}{\partial \zeta} \right) = \frac{1}{J} \left(-\frac{\partial y}{\partial \zeta}, \frac{\partial x}{\partial \zeta} \right), \tag{36}$$

so that the unit normal vectors can be defined as $\mathbf{n}_\zeta = \frac{\hat{\mathbf{n}}_\zeta}{|\hat{\mathbf{n}}_\zeta|}$ and $\mathbf{n}_\eta = \frac{\hat{\mathbf{n}}_\eta}{|\hat{\mathbf{n}}_\eta|}$. The infinitesimal lengths along the face on $\partial \Omega^e$ corresponding to ζ and η are

$$dl = |\epsilon_\zeta| = \left| \left(\frac{\partial x}{\partial \zeta}, \frac{\partial y}{\partial \zeta} \right) \right| d\zeta \quad \text{and} \quad dl = |\epsilon_\eta| = \left| \left(\frac{\partial x}{\partial \eta}, \frac{\partial y}{\partial \eta} \right) \right| d\eta, \tag{37}$$

respectively, and thus their associated surface Jacobians J^s are $\left| \left(\frac{\partial x}{\partial \zeta}, \frac{\partial y}{\partial \zeta} \right) \right|$ and $\left| \left(\frac{\partial x}{\partial \eta}, \frac{\partial y}{\partial \eta} \right) \right|$, respectively.

The semidiscrete scheme for Eq. (15) in a local domain Ω^e can be written in matrix form as:

$$\frac{d\mathbf{f}_\alpha}{dt} + \mathbf{M}^{-1} \mathbf{D} \mathbf{f}_\alpha = \mathbf{M}^{-1} \mathbf{R} \mathbf{f}_\alpha, \tag{38}$$

where $\mathbf{f}_\alpha = [\bar{f}_\alpha^N]_{ij}$ is a solution vector, $\mathbf{D} = e_{\alpha x} \mathbf{D}_x + e_{\alpha y} \mathbf{D}_y$, and \mathbf{R} is the surface integration acting on the boundary nodes on each face of the local element.

2.2.5. Eigenvalues of the SEDG operator

The semidiscrete SEDG scheme in Eq. (38) can be expressed in a simple form as:

$$\frac{d\mathbf{f}_\alpha}{dt} = \mathbf{L} \mathbf{f}_\alpha, \tag{39}$$

where $\mathbf{L} = \mathbf{M}^{-1}(-\mathbf{D} + \mathbf{R})$ is the spatial operator. To obtain a fully discrete scheme, we need to choose a method for integrating the system of the ordinary differential equations Eq. (39) in time. Let us denote the eigenvalues of the spatial operator as σ , satisfying $\mathbf{L} \mathbf{f}_\alpha = \sigma \mathbf{f}_\alpha$. For a fully discrete scheme to be stable, the real part of the eigenvalues must be $Re(\sigma) \leq 0$. Fig. 1 shows the eigenvalue spectrums of the spatial advection operator of the SEDG approximation for the central and Lax–Friedrichs fluxes with

periodic and wall boundary conditions. A uniform spectral element mesh is used with the number of elements $E = 3 \times 3$ and the approximation order $N = 5$.

For the case with periodic boundary conditions, all the eigenvalues of the advection operator with the central flux fall on the imaginary axis, while the eigenvalues of the advection operator for the Lax–Friedrichs flux are distributed in the negative half-plane. In Fig. 1(a) and (b), the maximum values of $Re(\sigma)$ indicate machine precision for both central and Lax–Friedrichs fluxes. This result indicates that one can choose the time-stepping scheme whose stability region includes the imaginary axis or negative half-plane for periodic problems.

For the case with wall boundary conditions, we observe some positive eigenvalues for the advection operator with the central flux. Fig. 1(c) shows that the maximum value of $Re(\sigma)$ is positive. Numerical solutions associated with the positive eigenvalues can grow dramatically in time, resulting in instability. Thus, central flux is not suitable for problems with wall boundary conditions. The spatial operator with the Lax–Friedrichs flux for wall boundary conditions has all the eigenvalues in the negative half-plane with a maximum value of $Re(\sigma)$ at machine precision, shown in Fig. 1(d). Thus one can choose a time-stepping scheme whose stability region includes the negative half-plane for the Lax–Friedrichs flux.

2.2.6. Timestepping method

For time integration, we choose the fourth-order, 5-stage, low-storage Runge–Kutta (RK) method [36] defined below, whose stability region is slightly larger and with less memory than those of the classical RK methods:

$$\begin{aligned}
 \mathbf{u}_0 &= \mathbf{f}_x^n \\
 i = 1, \dots, s (s = 5) : \mathbf{u}_j &= \sum_{j=0}^{i-1} a_{ij} \mathbf{u}_j + b_{ij} \delta t \mathbf{L}(\mathbf{u}_j, (n + c_j) \delta t) \\
 \mathbf{f}_x^{n+1} &= \mathbf{u}_s,
 \end{aligned}
 \tag{40}$$

where a_{ij} , b_{ij} , and c_j are given constants.

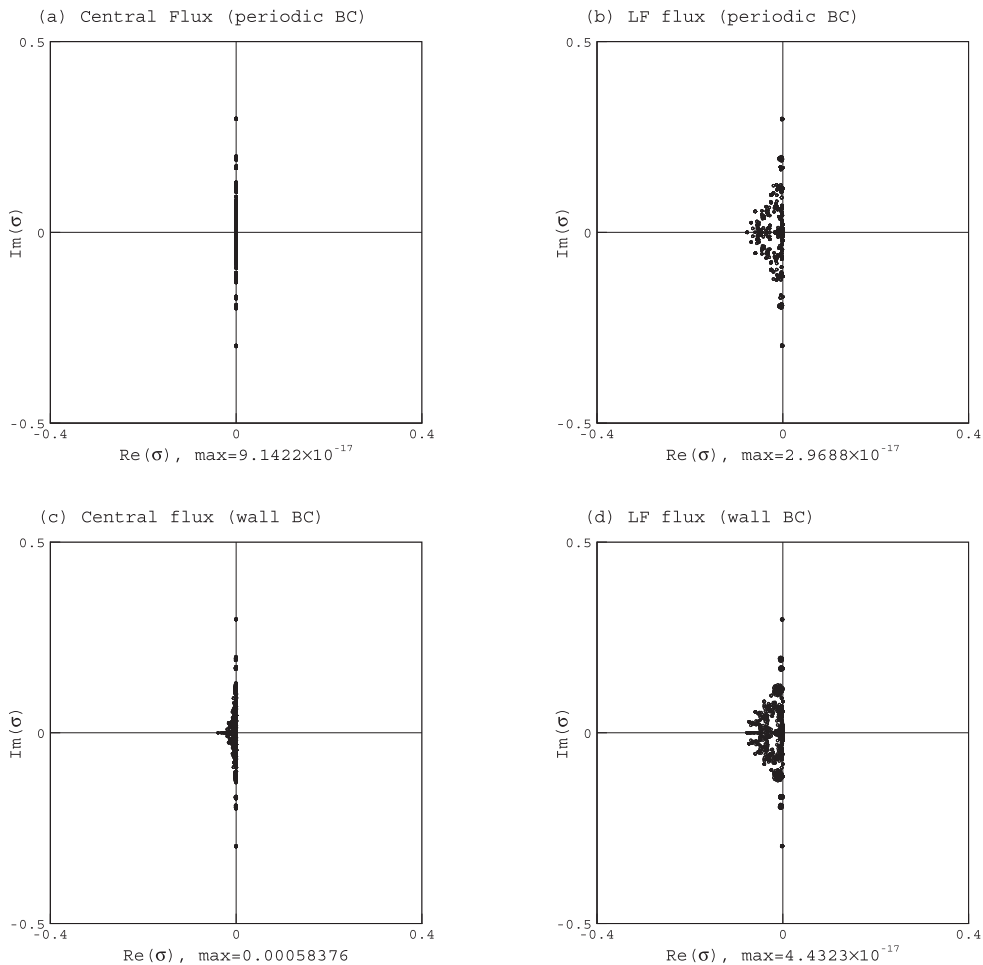


Fig. 1. Eigenvalue spectrums of the spatial advection operator based on the SEDG approximation with $E = 9, N = 5$ for (a) central flux with periodic boundary (b) Lax–Friedrichs flux with periodic boundary (c) central flux with wall boundary (d) Lax–Friedrichs flux with wall boundary conditions.

3. Computational results

In this section, we demonstrate convergence studies and test our SEDG-LBM over benchmark problems including unsteady Couette flows, lid-driven cavity flows, and flows past an impulsively started cylinder. As shown in the previous section, the central flux is not suitable for problems with wall boundary condition, and therefore only the Lax–Friedrichs flux is used in the benchmark calculations.

3.1. Convergence for unsteady Couette flow

We consider unsteady Couette flow on $[0, L]^2$. The top plate moves at a constant velocity $\mathbf{u}_b = (U, 0)$, and the bottom one is kept stationary. A periodic boundary condition is applied in the x -direction. The Reynolds number of the Couette flow is defined as $Re = UL/\nu$. One can obtain the analytic solution from the incompressible Navier–Stokes equations for the Couette flows that is defined as:

$$\mathbf{u}(y, t) = U \frac{y}{L} + \sum_{m=1}^{\infty} \frac{2U(-1)^m}{\lambda_m L} e^{-\nu \lambda_m^2 t} \sin(\lambda_m y), \tag{41}$$

for $\lambda_m = \frac{m\pi}{L}$, $m = 1, 2, 3, \dots$

The cases with $L = 1$ and $Ma = 0.05$ are examined. We use the total number of elements $E = 6 \times 6$ of equal size. Fig. 2 shows the spatial convergence of SEDG-LBM depending on $N = 2, 4, 6, 8, 10, 12,$ and 14 at time $t = 40$ with $Re = 2000$. The errors show exponential convergence as N increases until it is saturated by temporal error.

3.2. Lid-driven cavity flows

Steady-state flows inside a square lid-driven cavity are simulated by using our SEDG-LBM described in the previous section. The Reynolds number of the lid-driven cavity flow is UL/ν , where $U = c_s Ma$ is the velocity of the lid and L the length of the lid. We set the initial velocity \mathbf{u} as $(u_x, u_y) \equiv (0, 0)$ and the initial density $\rho \equiv 1$. At $t > 0$, we let the top lid move at the velocity $\mathbf{u}_b = (u_x, u_y) = (U, 0)$ with a Mach number $Ma = 0.1$. The velocity of the top lid is imposed through the numerical flux as described in Section 2.2.3.

Fig. 3 shows the streamlines of the cavity flows at $Re = 1000$ and $Re = 5000$ with the Lax–Friedrichs flux on a nonuniform spectral element mesh with $E = 256$. We used the polynomial order of $N = 5$ and a time-step δt such that $CFL = \frac{\max_x |e_x| \delta t}{\Delta x_{\min}} = 0.4$, where Δx_{\min} is the minimum grid spacing.

Fig. 4 demonstrates the nondimensional horizontal velocity u_x/U along the mid-vertical line of the cavity y/H , where H is the height of the cavity, for $Re = 400, 1000, 3200,$ and 5000 from our SEDG-LBM simulations, keeping the mesh resolution constant as in Fig. 3 with the total number of grids $\mathcal{N} = (N + 1)^2 E = 36 \times 256$. A good agreement at high Re is particularly notable with fewer grid points when compared to the Ghia et al.'s simulations [37] using an implicit multigrid method.

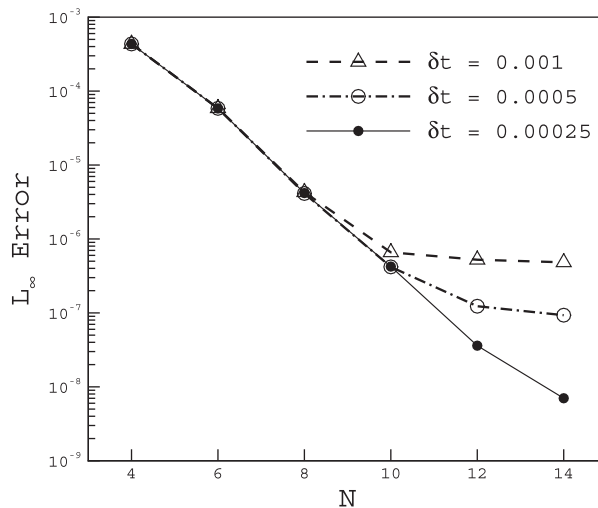


Fig. 2. Spatial convergence for the unsteady Couette flow with different δt for a fixed $Re = 2000$.

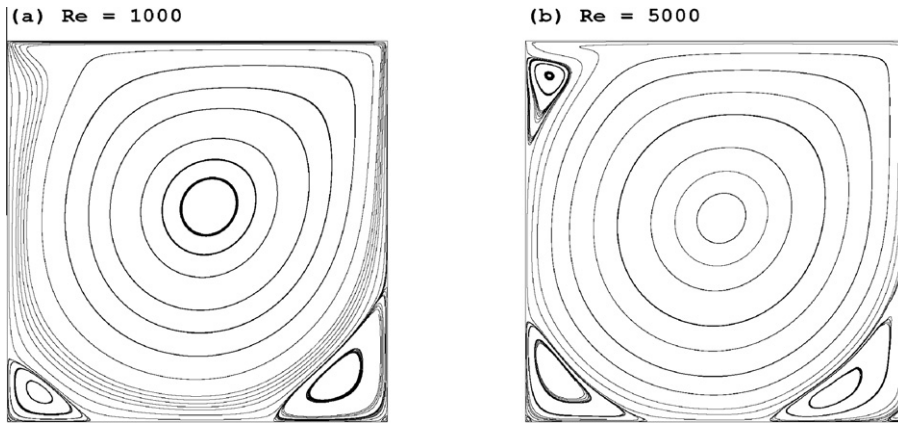


Fig. 3. Streamlines of the cavity flow at (a) $Re = 1000$ and (b) $Re = 5000$ with the Lax–Friedrichs flux for $E = 256$ and $N = 5$, with the total grids $\mathcal{N} = (N + 1)^2 E$.

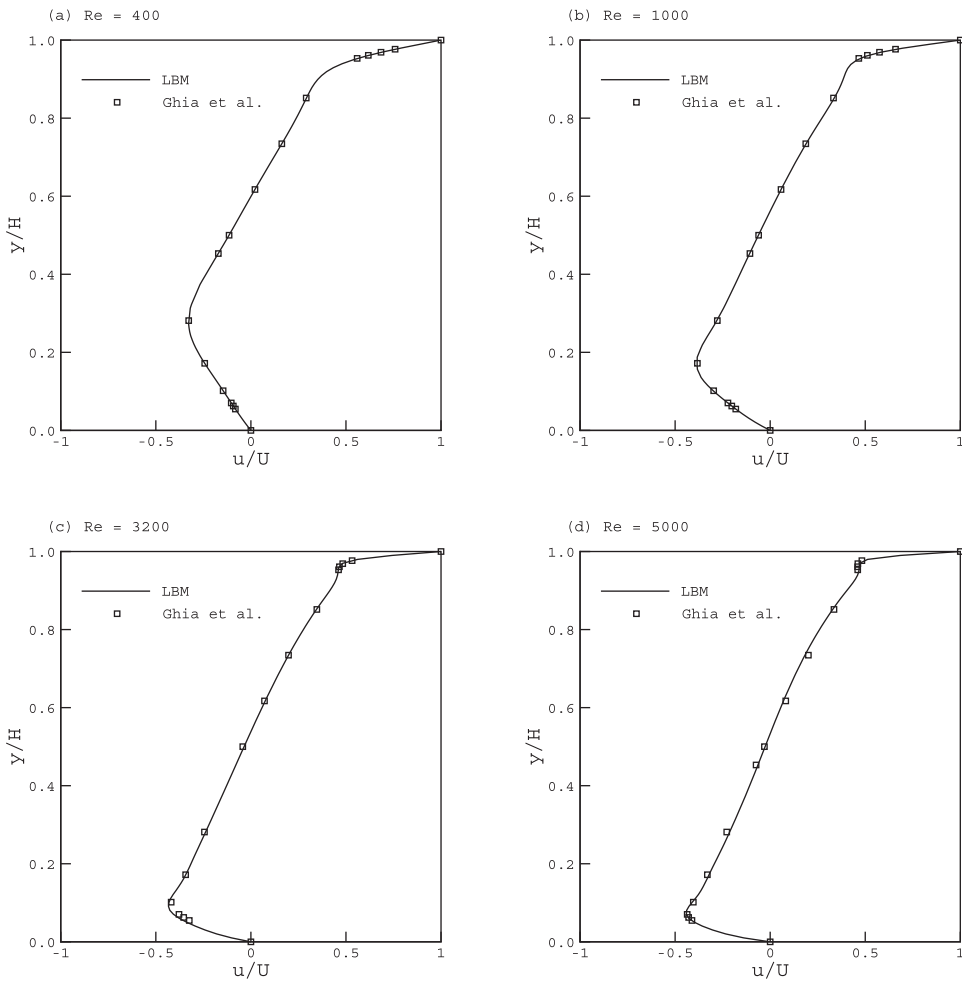


Fig. 4. Nondimensional horizontal velocity (u/U) along mid-vertical line for $Re = 400, 1000, 3200,$ and 5000 . Lines represent our SEDG-LBM results, and square dots represent the results by an implicit multigrid method by Ghia et al. [37].

3.3. Flow past an impulsively started cylinder

In this section, time evolution of flows around an impulsively started circular cylinder is considered; and boundary-layer development, separation, and drag forces are studied in detail. The computational results are compared mainly with those from the vortex method and the spectral element method associated with the incompressible Navier–Stokes equations [38,39]. High-resolution simulations are necessary at high Re to adequately resolve the singular character of the flow at early times and to resolve the details of the separation process [40–42]. At $t = 0^+$, it is assumed that a potential flow exists, and a

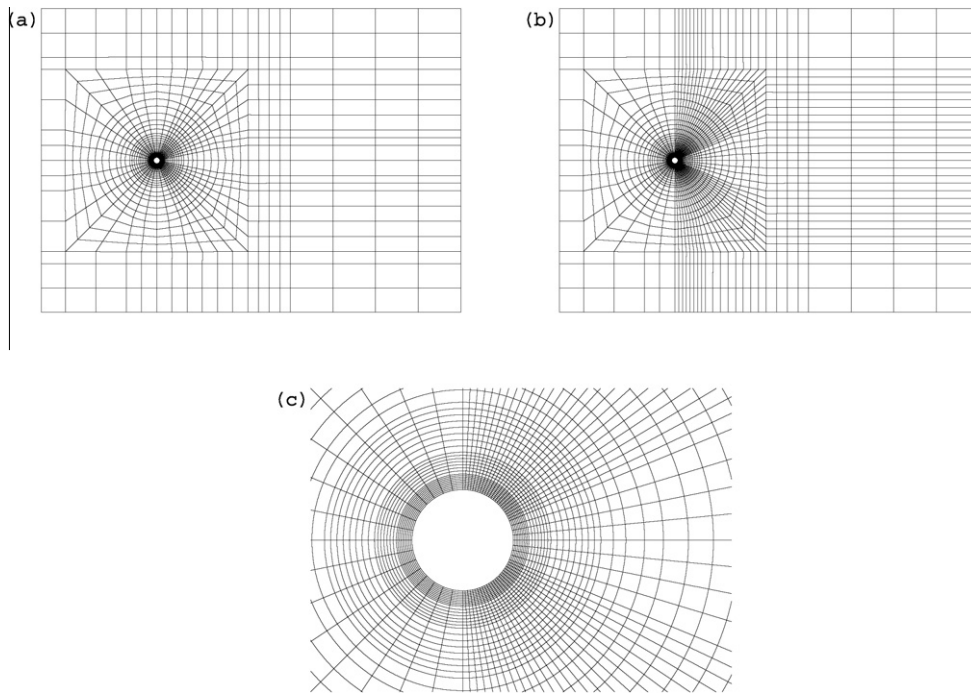


Fig. 5. Spectral element mesh around a circular cylinder with (a) $E = 2,208$ and (b) $E = 3,758$. (c) Close-up view around the cylinder for $E = 3,758$. Cylinder diameter $D = 1.0$, and computational domain $\Omega = [-19, 50] \times [-25, 25]$.

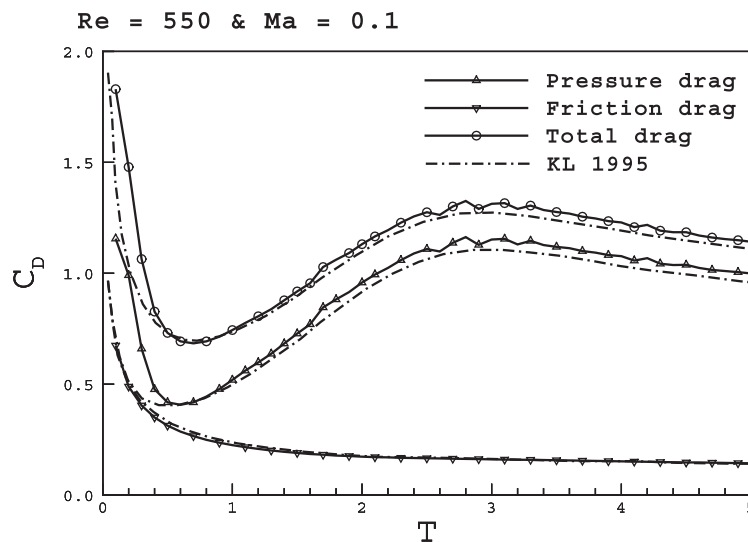


Fig. 6. Time evolution of the drag coefficients for $Re = 550$ and $Ma = 0.1$ with $E = 2,208$, $N = 5$, and $\mathcal{N} = 6^2 \times 2,208$ for SEDG-LBM. Dash-dotted line presents the results from the vortex method by Koumoutsakos and Leonard [38].

slip velocity (vortex sheet of zero thickness) is observed on the surface of the body. Numerical schemes encounter difficulties in resolving the initially developed thin boundary layers associated with impulsive starts and in computing accurately quan-

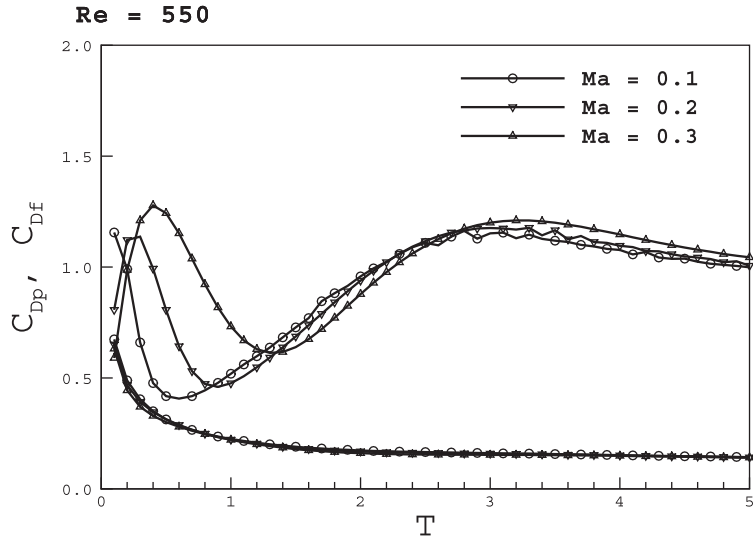


Fig. 7. Time evolution of the pressure and friction drag coefficients for $Ma = 0.1, 0.2,$ and 0.3 with $E = 2,208, N = 5,$ and $\mathcal{N} = 6^2 \times 2,208$ for SEDG-LBM.

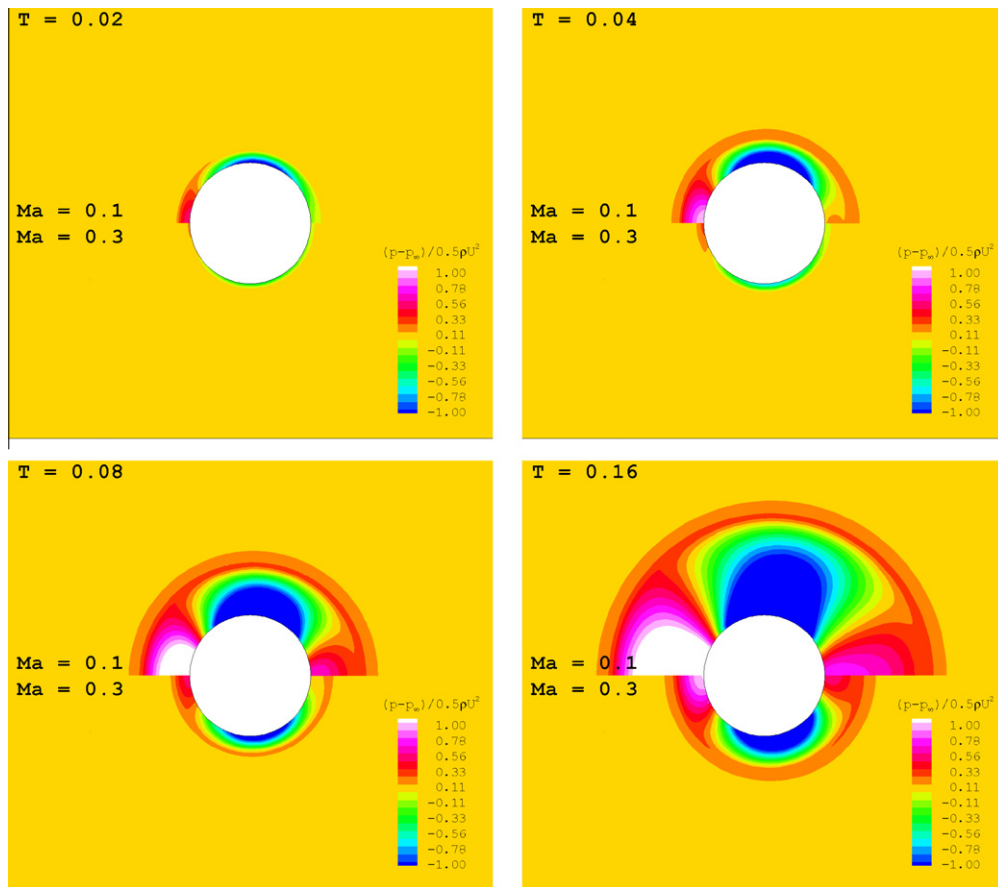


Fig. 8. Sequence of contour plots of the pressure wave $(p - p_\infty) / (\frac{1}{2} \rho U^2)$ for $Re = 550$ at $T = 0.02, 0.04, 0.08,$ and 0.16 with $E = 2,208, N = 5,$ and $\mathcal{N} = 6^2 \times 2,208$ for SEDG-LBM. Upper and lower halves represent SEDG-LBM simulations at $Ma = 0.1$ and $Ma = 0.3,$ respectively.

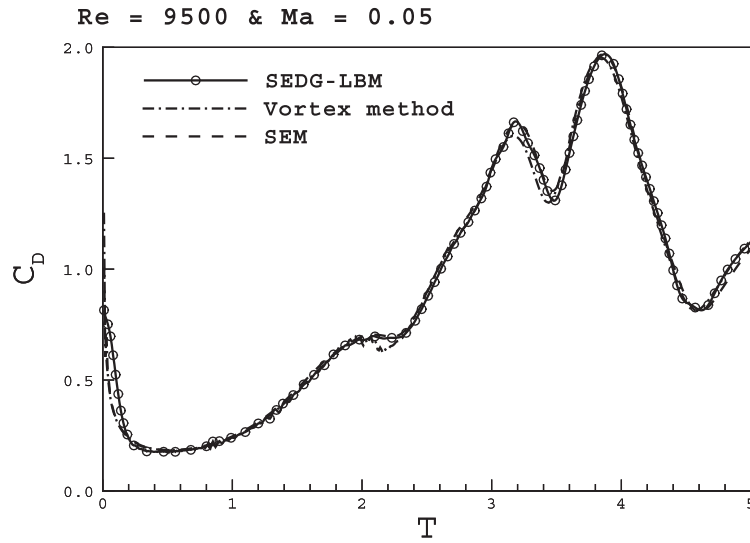


Fig. 9. Time evolution of the drag coefficients for $Re=9500$ and $Ma=0.05$ computed on a mesh with $E=3,758$, $N=5$, and $\mathcal{N} = (N+1)^2 E = 6^2 \times 3,758 = 135,288$ for SEDG-LBM. Dash-dotted line presents the results obtained from the vortex method [38], and the dashed line the results from the spectral element simulations [39].

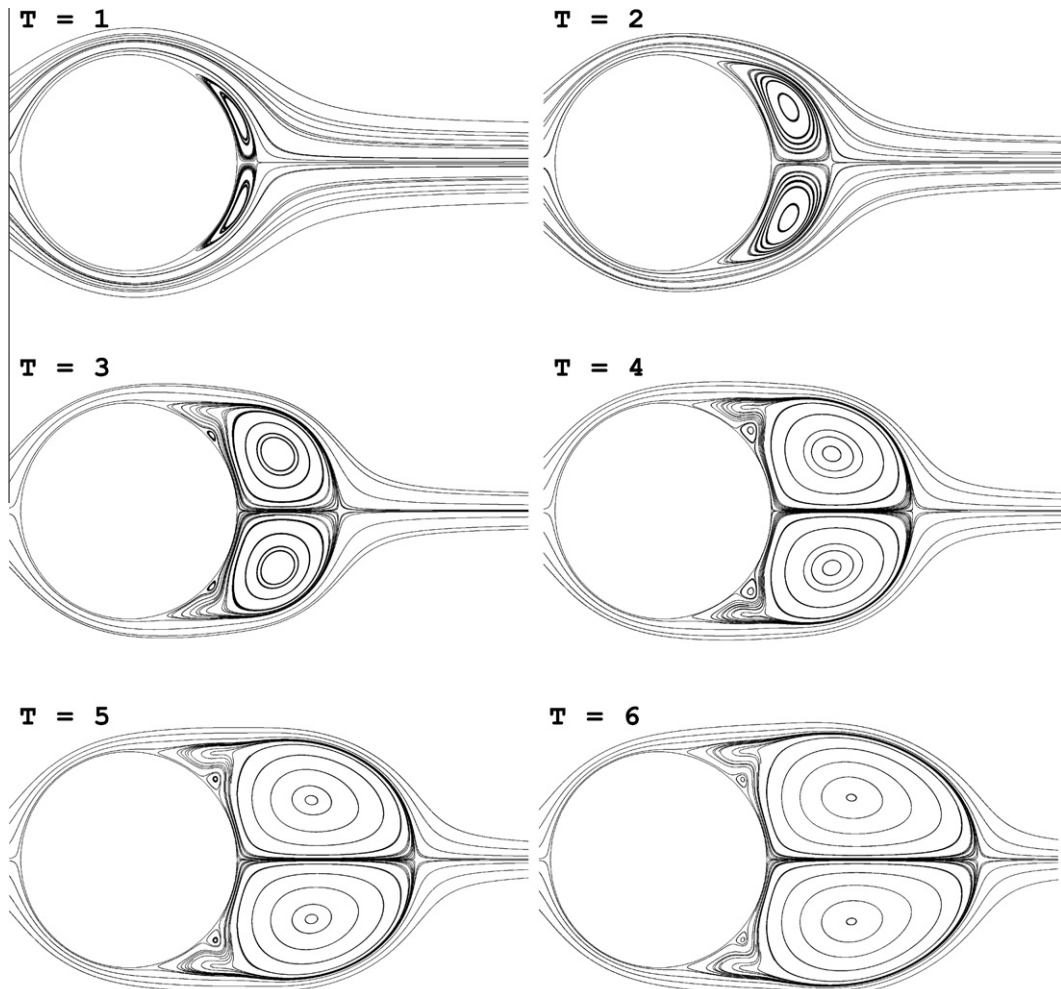


Fig. 10. Time evolution of streamlines at $Re = 550$ and $Ma = 0.1$; $E = 2,208$, $N = 5$ and $\mathcal{N} = (N+1)^2 E$.

tities such as the drag coefficient. At $t > 0$ we impose $\mathbf{u}_b = (u_x, u_y) = (0, 0)$ on the surface of the cylinder. The boundary conditions are imposed weakly through the numerical flux as described in Section 2.2.3.

The Reynolds number of the flow is

$$Re = \frac{U_\infty D}{\nu}, \tag{42}$$

where U_∞ is the uniform inlet velocity and D is the diameter of the cylinder. The dimensionless time T is based on the radius of the cylinder:

$$T = \frac{2U_\infty t}{D}. \tag{43}$$

Computations are carried out for $Re = 550$ and 9500 with $CFL = 0.4$. Fig. 5 shows a spectral element mesh with $E = 2,208$. The total drag force on the cylinder, $\bar{\mathbf{F}}_t$, is

$$\bar{\mathbf{F}}_t = \bar{\mathbf{F}}_p + \bar{\mathbf{F}}_f, \tag{44}$$

where $\bar{\mathbf{F}}_p$ is the force due to pressure and $\bar{\mathbf{F}}_f$ the force due to friction. The total drag coefficient of the cylinder, C_D , is

$$C_D = \frac{\bar{\mathbf{F}}_t \cdot \mathbf{i}}{\frac{1}{2} \rho_\infty U_\infty^2 D}, \tag{45}$$

where \mathbf{i} is the unit vector in the x -direction. The pressure and friction drag coefficients, C_{Dp} and C_{Df} , are defined in a similar manner.

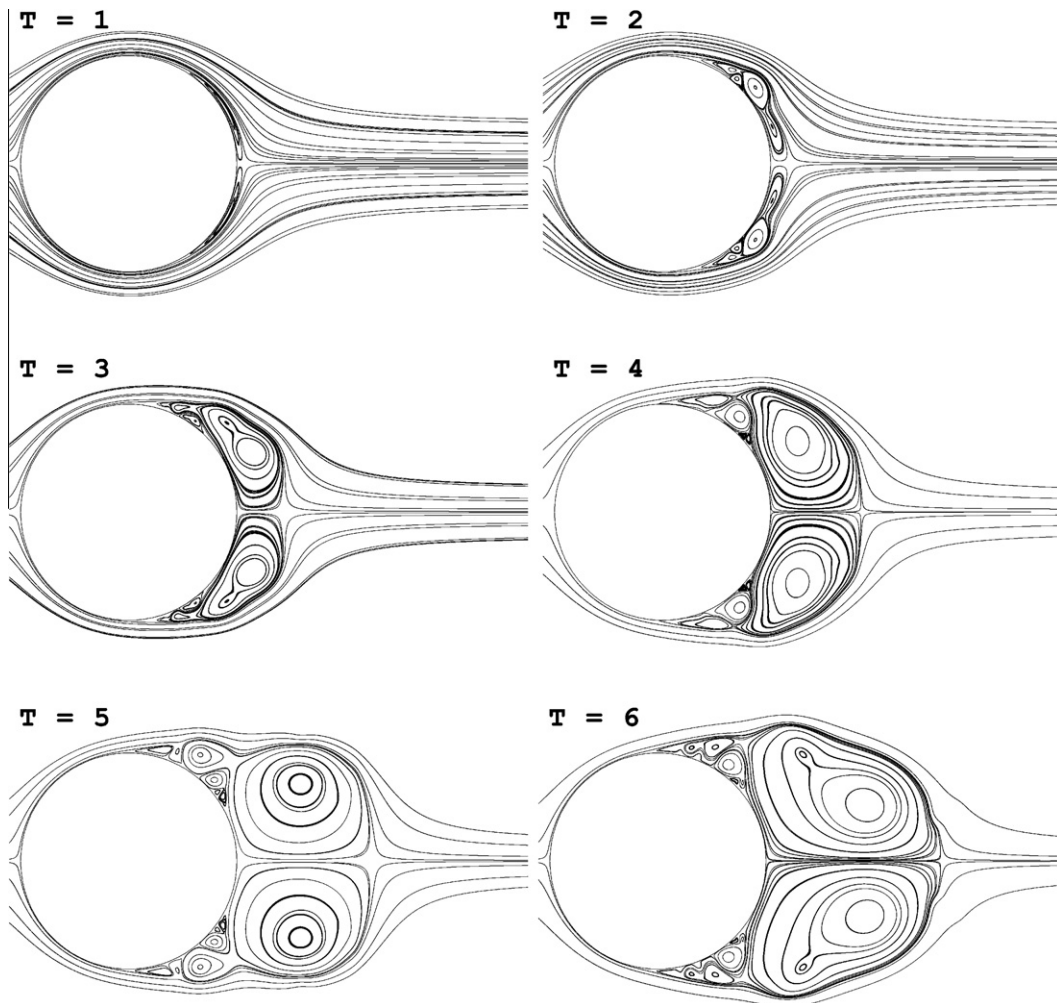


Fig. 11. Time evolution of streamlines at $Re = 9500$ and $Ma = 0.05$; $E = 3,758$, $N = 5$, and $\mathcal{N} = (N + 1)^2 E$.

In Fig. 6, time evolution of the pressure, friction, and total drags is compared to their time evolution with the vortex method by Koumoutsakos and Leonard [38]. At earlier times for $T < 0.5$, the vortex method gives a much more rapid decrease of the pressure and total drags, exhibiting a $t^{1/2}$ singularity [41]. The friction drag coefficient of our SEDG-LBM agrees well with that obtained by the vortex method. The drag coefficients gradually recover from the sudden drop due to the impulsive start, and SEDG-LBM results start to show good agreement with the vortex method for $T \geq 1$, when the effects of convection become important. As noted first in [41], the results from our SEDG-LBM shows a slower decay mainly because of its finite-compressibility effect.

In Fig. 7, we show the drag coefficients for $Ma = 0.1, 0.2$, and 0.3 . Clearly, as Ma increases, the initial decay in the pressure drag coefficient slows, and the recovery from a sudden drop due to the impulsive start is delayed. We note that the friction drag coefficient is not very sensitive to the variation of Ma . This result implies that the compressibility in LBM affects mostly the pressure field. The pressure wave originating from the impulsive start travels at a constant lattice speed of sound c_s . Since dimensionless time is measured with flow velocity U_∞ , the distance traveled by the pressure wave is inversely proportional to Ma at a given time.

Fig. 8 shows the sequence of contour plots of the dimensionless pressure wave defined as $(p - p_\infty) / (\frac{1}{2} \rho U_\infty^2)$ for $Ma = 0.1$ and $Ma = 0.3$ with constant reference pressure p_∞ . Initially at $T = 0$, the pressure field is uniform. The pressure wave with $Ma = 0.1$ propagates from the cylinder surface three times faster than the one with $Ma = 0.3$ and disappears much more quickly from the cylinder. The nearly incompressible pressure field, in which the front stagnation point has the highest value and the top and bottom surfaces of cylinder have lower values, is slowly established as the pressure wave propagates outward radial direction. As the pressure at the front stagnation point is increased, the pressure drag increases until $T < 0.5$ (Fig. 7), which takes less time for smaller Ma . Once the pressure field is recovered, the pressure drag starts to decrease and then gradually increases.

In Fig. 9, we present the results of drag coefficient in comparison with those of the vortex method [38] and the spectral element method (SEM) [39]. Our grid resolution is $135,288$ ($E = 3,758, N = 5$) for $Re = 9500$ and $Ma = 0.05$. The results show good agreement with the results from the vortex method and SEM. The delay in establishing the incompressible pressure field around the cylinder contributes to the discrepancy in the pressure drag coefficients at early time between the results from SEDG-LBM, the vortex method, and SEM, as shown in Fig. 9.

Figs. 10 and 11 demonstrate the time sequence of streamlines with $Ma = 0.1$ for $Re = 550$ and $Re = 9500$ at different times T . The number of spectral elements $E = 2,208$ and $E = 3,758$, respectively for $Re = 550$ and $Re = 9500$, and the polynomial order of $N = 5$ are used.

4. Conclusions

We have presented a spectral-element discontinuous Galerkin lattice Boltzmann method for solving incompressible flows, such as the flows for a lid-driven cavity and an impulsively started cylinder. We decoupled the lattice Boltzmann equation into collision and streaming steps, giving flexibility in dealing with numerical stability at high Reynolds numbers. In the streaming step, we used a spectral element discretization in a discontinuous Galerkin form with a fully diagonal mass matrix for solving the advection equation. We have shown the implementation for imposing boundary conditions weakly through numerical fluxes, especially Lax–Friedrichs flux.

We have examined lid-driven cavity flows for $Re = 400$ – 5000 and flows around an impulsively started cylinder for $Re = 550$ – 9500 . Computational results show good agreement with the results from previously studied methods, namely, an implicit multigrid method, a vortex method, and a spectral element method. Our method shows some delay in establishing incompressibility at the initial stage of the simulation due to its inherent weak compressibility at larger Ma . From the computational experiments, we have demonstrated our SEDG-LBM delivers accuracy and efficiency for simulations of unsteady complex flows. Extension to three dimensions and performance studies in comparison to other approaches remain as a future work.

Acknowledgments

This work was partially supported by the Office of Advanced Scientific Computing Research, Office of Science, U.S. Department of Energy, under Contract DE-AC02-06CH11357, and partially by the National Science Foundation grant DMS-0811046 and Nuclear Regulatory Commission grant NRC-38-09-947. The authors thank Paul Fischer for his helpful discussions and providing his drag coefficient data for SEM.

References

- [1] D.A. Wolf-Gladrow, Lattice-Gas Cellular Automata and Lattice Boltzmann Models: An Introduction, Lecture Notes in Mathematics, Springer, Berlin, 2000.
- [2] S. Succi, The Lattice Boltzmann Equation: For Fluid Dynamics and Beyond, Oxford University Press, 2001.
- [3] X.Y. He, L.-S. Luo, Lattice Boltzmann model for the incompressible Navier–Stokes equation, J. Stat. Phys. 88 (1997) 927–944.
- [4] X. He, L.-S. Luo, Theory of the lattice Boltzmann method: from the Boltzmann equation to the lattice Boltzmann equation, Phys. Rev. E 53 (1997) 6811–6817.

- [5] T. Abe, Derivation of the lattice Boltzmann method by means of the discrete ordinate method for the Boltzmann equation, *J. Comput. Phys.* 131 (1997) 241–246.
- [6] N. Cao, S. Chen, S. Jin, D. Martinez, Physical symmetry and lattice symmetry in the lattice Boltzmann method, *Phys. Rev. E* 55 (1997) R21.
- [7] G.R. McNamara, A.L. Garcia, B.J. Alder, Stabilization of thermal lattice Boltzmann models, *J. Stat. Phys.* 81 (1995) 395–408.
- [8] X. He, L.-S. Luo, M. Dembo, Some progress in lattice Boltzmann method. Part I. Nonuniform mesh grids, *J. Comput. Phys.* 129 (1996) 357–363.
- [9] R. Mei, W. Shyy, On the finite difference-based lattice Boltzmann method in curvilinear coordinates, *J. Comput. Phys.* 143 (1998) 426–448.
- [10] R. Zhang, H. Chen, Y.H. Qian, S. Chen, Effective volumetric lattice Boltzmann scheme, *Phys. Rev. E* 63 (2001) 056705.
- [11] V. Sofonea, R.F. Seikerka, Viscosity of finite difference lattice Boltzmann models, *J. Comput. Phys.* 184 (2003) 422–434.
- [12] A. Bardow, I.V. Karlin, A.A. Gusev, General characteristic-based algorithm for off-lattice Boltzmann simulations, *Europhys. Lett.* 75 (2006) 434–440.
- [13] T. Lee, C.-L. Lin, L.-D. Chen, A lattice Boltzmann algorithm for calculation of the laminar jet diffusion flame, *J. Comput. Phys.* 215 (2006) 133–152.
- [14] H. Xi, G. Peng, S.-H. Chou, Finite volume lattice Boltzmann method, *Phys. Rev. E* 59 (1999) 6202.
- [15] S. Ubertini, G. Bella, S. Succi, Unstructured lattice Boltzmann method: further development, *Phys. Rev. E* 68 (2003) 016701.
- [16] M. Stiebler, J. Tölke, M. Krafczyk, An upwind discretization scheme for the finite volume lattice Boltzmann method, *Comput. Fluids* 35 (2006) 814–819.
- [17] F. Dubois, P. Lallemand, On lattice Boltzmann scheme, finite volumes and boundary conditions, *Prog. Comput. Fluid Dyn.* 8 (2008) 11–24.
- [18] V. Patil, K.N. Lakshminisha, Finite volume TVD formulation of lattice Boltzmann simulation on unstructured mesh, *J. Comput. Phys.* 228 (2009) 5262–5279.
- [19] T. Lee, C.-L. Lin, A characteristic Galerkin method for discrete Boltzmann equation, *J. Comput. Phys.* 171 (2001) 336–356.
- [20] T. Lee, C.-L. Lin, An Eulerian description of the streaming process in the lattice Boltzmann equation, *J. Comput. Phys.* 185 (2003) 445–471.
- [21] Y. Li, E.J. LeBoeuf, P.K. Basu, Least-squares finite-element scheme for the lattice Boltzmann method on an unstructured mesh, *Phys. Rev. E* 72 (2005) 046711.
- [22] X. Shi, J. Lin, Z. Yu, Discontinuous Galerkin spectral element lattice Boltzmann method on triangular element, *Int. J. Numer. Meth. Fluids* 42 (2003) 1249–1261.
- [23] A. Düster, L. Demkowicz, E. Rank, High-order finite elements applied to the discrete Boltzmann equation, *Int. J. Numer. Meth. Eng.* 67 (2006) 1094–1121.
- [24] T. Lee, G.K. Leaf, Eulerian description of high-order bounce-back scheme for lattice Boltzmann equation with curved boundary, *Eur. Phys. J. Special Topics* 171 (2009) 3–8.
- [25] C. Pan, L.-S. Luo, C.T. Miller, An evaluation of lattice Boltzmann scheme for porous medium flow simulation, *Comput. Fluids* 35 (2006) 898–909.
- [26] B. Chun, A.J.C. Ladd, Interpolated boundary condition for lattice Boltzmann simulations of flows in narrow gaps, *Phys. Rev. E* 75 (2007) 066705.
- [27] J.S. Hesthaven, T. Warburton, Nodal discontinuous Galerkin methods, algorithms, analysis, and applications, *Texts in Applied Mathematics*, Springer, 2008.
- [28] X. He, Q. Zou, L.-S. Luo, M. Dembo, Analytic solutions of simple flows and analysis of nonslip boundary conditions for the lattice Boltzmann BGK model, *J. Stat. Phys.* 87 (1997) 115–136.
- [29] P.L. Bhatnagar, E.P. Gross, M. Krook, A model for collision processes in gases, I: Small amplitude processes in charged and neutral one-component system, *Phys. Rev.* 94 (1954) 511–525.
- [30] Y.H. Qian, D. D’Humières, P. Lallemand, Lattice BGK models for Navier–Stokes equation, *Europhys. Lett.* 17 (1992) 479–484.
- [31] X. He, S. Chen, G.D. Doolen, A novel thermal model for the lattice Boltzmann method in incompressible limit, *J. Comput. Phys.* 146 (1998) 282–300.
- [32] F.X. Giraldo, M. Restelli, A study of spectral element and discontinuous Galerkin methods for the Navier–Stokes equations in nonhydrostatic atmospheric modeling: equation sets and test cases, *J. Comput. Phys.* 227 (2008) 3849–3877.
- [33] F.X. Giraldo, T. Warburton, A triangular discontinuous Galerkin oceanic shallow water model, *Int. J. Numer. Meth. Fluids* 56 (2008) 899–925.
- [34] M.O. Deville, P.F. Fischer, E.H. Mund, *High-order Methods for Incompressible Fluid Flow*, Cambridge Monographs on Applied and Computational Mathematics, Cambridge University Press, 2002.
- [35] J.S. Hesthaven, S. Gottlieb, D. Gottlieb, *Spectral Methods for Time-dependent Problems*, Cambridge Monographs on Applied and Computational Mathematics, Vol. 21, Cambridge University Press, 2007.
- [36] M.H. Carpenter, C. Kennedy, Fourth-order 2N-storage Runge–Kutta schemes, NASA Report TM 109112, NASA Langley Research Center (1994).
- [37] U. Ghia, K.N. Ghia, C.T. Chin, High *Re* solutions for incompressible flow using the Navier–Stokes equation and multigrid methods, *J. Comput. Phys.* 48 (1982) 387–411.
- [38] P. Koumoutsakos, A. Leonard, High-resolution simulations of the flow around an impulsively started cylinder using vortex methods, *J. Fluid Mech.* 296 (1995) 1–38.
- [39] P.F. Fischer, An overlapping Schwarz method for spectral element solution of the incompressible Navier–Stokes equations, *J. Comput. Phys.* 133 (1997) 84–101.
- [40] X.D. Niu, Y.T. Chew, C. Shu, Simulation of flows around an impulsively started circular cylinder by Taylor series expansion- and least squares-based lattice Boltzmann method, *J. Comput. Phys.* 188 (2003) 176–193.
- [41] Y. Li, R. Shock, R. Zhang, H. Chen, Numerical study of flow past an impulsively started cylinder by the lattice-Boltzmann method, *J. Fluid Mech.* 519 (2004) 273–300.
- [42] A. Dupuis, P. Chatelain, P. Koumoutsakos, An immersed boundary-lattice-Boltzmann method for the simulation of the flow past an impulsively started cylinder, *J. Comput. Phys.* 227 (2008) 4486–4498.